

Application of DInSAR technique for post-earthquake land deformation mapping of Eastern Nepal

The 25 April 2015 earthquake (also known as Gorkha earthquake) occurred at 11:56 NST, with a magnitude of 7.8 in Gorkha district in Nepal with hypocentre at a depth of approximately 15 km. The earthquake was followed by continued aftershocks with second major earthquake of magnitude 7.3 in Nepal on 12 May 2015 at 12:50 pm. The epicentre of the first earthquake was at 28.147°N and 84.708°E. The epicentre of the second one was near the Chinese border between Kathmandu and Mt. Everest at the location 27.837°N and 86.077°E and on the border of Dolakha and Sindhupal chowk districts of Nepal. This earthquake occurred on the same fault as the larger magnitude 7.8 earthquake of 25 April, but further east. The effect of this earthquake was so strong that the shaking was felt in northern parts of India also including Bihar, Uttar Pradesh and West Bengal. Figure 1 shows the map of Nepal along with the epicentre locations of 25 April earthquake and 12 May earthquake.

The focal mechanism of the main shock, i.e. Gorkha earthquake has been studied and analysed¹. This event occurred by slip on a ~150 km long and 55 km wide, shallow dipping (~5°) segment of the Main Himalayan Thrust (MHT), causing the Himalaya to lurch southwestward by 4.8 ± 1.2 m over the Indian plate¹. The rupture area of the main shock overlaps the meioseismal zone of the 1833 Nepal earthquake and is immediately to the west of the 1934 Bihar–Nepal earthquake. This region had accumulated ~3 m of slip in the past 182 years, converging at a rate of ~18 mm/yr¹.

In the present study, we have used differential interferometry (DInSAR) technique and C-band Sentinel-1 Interferometric Wide Swath SLC (IW-SLC), VV polarization data for post-earthquake land deformation mapping of eastern Nepal. Interferometric Synthetic Aperture Radar (InSAR) is the technique to measure the phase change between the two radar images taken from the same sensor at two different times. InSAR has been used to measure deformations of the earth's surface since the eighties². Studies have been made to monitor the consequences of earthquakes, volcanism, oil or gas extraction, groundwater flow, ice

motion and geo-technical processes using the DInSAR approach. It refers to the process, where a pair of images is used for the interferometric analysis to identify and quantify the surface movement³. The word 'differential' implies the subtraction of the topographic phase contribution from the SAR interferogram.

Table 1 gives the details of the data used. Sentinel-1 space mission is a part of Copernicus Programme of European Space Agency (ESA) consisting of a constellation of two identical satellites operating at 180° globally apart⁴. Sentinel-1A was launched on 3 April 2014 on a Soyuz rocket from Europe's Spaceport in French Guiana. For subtraction of the phase due to topography, SRTM 90 m elevation data has been used.

Using the pre-earthquake and post-earthquake Sentinel-1 SLC data, interferograms were generated for the pairs 24 April 2015–6 May 2015 (for April earthquake) and for 6 May 2015–18 May

2015 (for May earthquake). For importing and processing of the Sentinel-1 data SARscape 5.1 module was used. Interferogram was generated by multiplying the master image with the complex conjugate of the slave image. The interferogram generated contains the information of phase difference. In order to remove the topography-related fringes, external SRTM 90 m elevation data was used and differential interferogram was generated. Differential interferogram was filtered and phase unwrapping was performed using minimum cost flow (MCF) method⁵. For the correct transformation of the unwrapped phase information into displacement values, refinement and re-flattening step was carried out. It allows both to refine the orbits (i.e. correcting possible inaccuracies) and to calculate the phase offset (i.e. getting the absolute phase values), or remove possible phase ramps. The absolute calibrated and unwrapped phase values were then converted

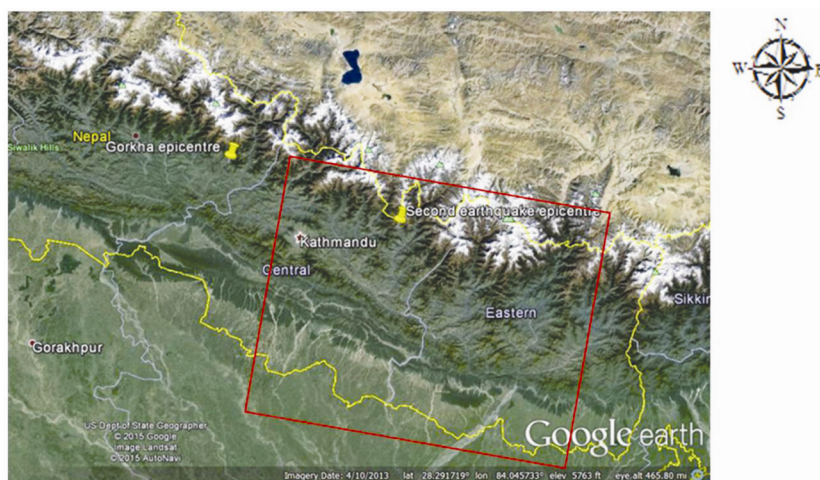


Figure 1. Map of Nepal showing the location of epicentre (shown as yellow placemarks) of Gorkha earthquake and 12 May 2015 Nepal earthquake (courtesy, Google Earth).

Table 1. Details of the Sentinel-1 data used

Date of acquisition of master image	24 April 2015	6 May 2015
Radar center frequency	5.405 GHz	5.405 GHz
Date of acquisition of slave image	6 May 2015	18 May 2015
Normal baseline (m)	224.28	-44.26
Temporal cycle	12 days	12 days
Critical baseline (m)	-5660.34	-5682.67
2pi ambiguity height (m)	69.21	351.78
2pi ambiguity displacement (m)	0.028	0.028

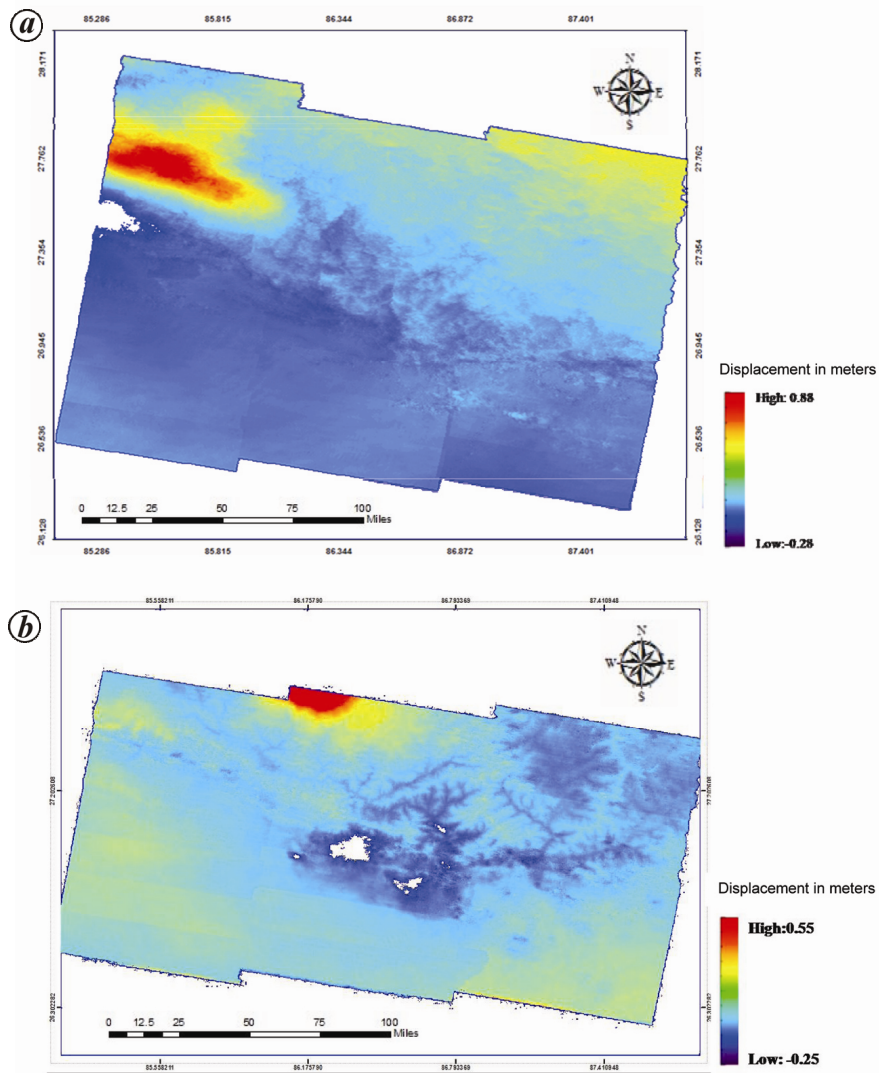


Figure 2. Land displacement map of eastern part of Nepal due to (a) Gorkha earthquake on 25 April 2015 and (b) due to 12 May 2015 earthquake.

to displacement and directly geo-coded into a map projection. This step is performed in a similar way as in the geocoding procedure by considering the Range–Doppler approach and the related geodetic and cartographic transforms. In a DInSAR interferogram, a complete phase cycle (i.e. 2π radian phase difference) or fringe represents radar line-of-sight ground displacement of $\lambda/2$, where λ is the radar wavelength being used. For example, in the case of C-band radar ($\lambda = 5.6$ cm), each fringe represents 2.8 cm or 28 mm radar line-of-sight displacement. In 2-pass approach we used SRTM elevation data for subtraction of topography-related phase. Any error associated with DEM will propagate into the deformation results. The phase

change associated with the change in topographic height is given as⁶

$$\Delta\phi = \frac{4\pi}{\lambda} \frac{B_{\perp}}{R \sin\theta} \Delta h, \quad (1)$$

where B_{\perp} is normal baseline, R the distance from SAR to scatterer, θ is look angle.

For calculating the standard error due to SRTM DEM, first the change in height due to 2π phase change was calculated as

$$dh = \frac{\lambda r \sin\theta}{4\pi B_{\perp}} \times 2\pi. \quad (2)$$

Hence, the standard DInSAR error due to SRTM DEM error will be

$$\text{DInSAR error} = \frac{\lambda \times \text{SRTM DEM error}}{2 \times dh}. \quad (3)$$

Slant range land deformation maps generated are shown in Figure 2 a and b for April and May earthquakes respectively. For Gorkha earthquake, the slant range displacement was found to be in the -28 to 88 cm range, whereas for 12 May 2015 earthquake, it was in the -25 to 55 cm range. The standard error associated with inaccurate DEM was calculated as 0.64 cm, i.e. error due to 16 m vertical error of SRTM DEM and 0.13 cm respectively for April and May earthquakes. This error is very less and will not affect much the land displacement values. Kathmandu city in the north-east part in

Figure 2a shows uplift (red colour), whereas in Figure 2 the uplift is seen in the northern part of the displacement map which is near to the epicentre of May earthquake. The subsidence is shown by blue colour in both the maps. The results are in accordance to the results reported by the European Space Agency's 'SEOM programme-InSAR ap project' team and Advanced Rapid Imaging and Analysis (ARIA) team at JPL and Caltech^{7,8}.

1. Mitra, S., Paul, H., Ajay Kumar, Singh, S. K., Dey, S. and Powali, D., *Curr. Sci.*, 2015, **108**(10), 1938–1943.
2. Gabriel, A. K., Goldstein, R. M. and Zebker, H. A., *J. Geophys. Res.*, 1989, **94**(B7), 9183–9191.

3. Hanssen, R. F., *Data Interpretation and Error Analysis*, Kluwer Academic, Dordrecht, 2001.
4. <https://sentinel.esa.int/web/sentinel/user-guides/sentinel-1-sar> (last accessed on 21 May 2015).
5. Costantini, M., *IEEE Trans. Geosci. Remote Sens.*, 1998, **36**(3), 813–821.
6. Bamler, R. and Hartl, P., *Inverse Problems*, 1998, **14**, R1–R54.
7. <http://insarap.org> (last accessed on 26 September 2015).
8. http://aria.jpl.nasa.gov/case_studies (last accessed on 26 September 2015).

ACKNOWLEDGEMENTS. We thank Sri Tapan Misra, Director SAC for his encouragement; P. K. Pal (Deputy Director), Dr B. S. Gohil (Group Director, ADVG EPSA, SAC, ISRO) for their constant support. We also thank European Space agency (ESA) for

providing Sentinel-1 data of Nepal and the SARMAP team for providing evaluation version of SARscape 5.1.

Received 4 August 2015; revised accepted 9 October 2015

SHWETA SHARMA^{1,2,*}
Y. S. RAO²
AJAI¹
A. K. MATHUR¹

¹Space Applications Centre (ISRO), Ahmedabad 380 058, India

²Indian Institute of Technology Bombay, Mumbai 400 076, India

*For correspondence.

e-mail: shweta@sac.isro.gov.in

Secondary craters detection from Mini-SAR for lunar surface age dating

Counting of crater is a widely accepted method for estimation of geologic age where there is no returned lunar sample. For lunar landing site, cratering chronology and cratering rate decay are interpreted by the empirical relationship established by plotting crater frequency versus radiometric age¹. Surface age is determined by the observed crater size frequency distribution (CSFD) of a unit area to the production function (PF) and using the crater frequency together with a calibrated chronology function (CF). Impact craters are taken into account for dating using the crater diameter to its frequency present in an area. Impact craters result from interplanetary bombardment on the lunar surface. Lunar craters created by impact are labelled into primary and secondary craters. Primary impact craters are formed by direct meteoritic bombardment on the lunar surface. Secondary craters are formed from ejecta emitted from the primary crater. Surface age dating by CSFD technique has been used in high spatial resolution optical remote sensing datasets like the Terrain Mapping Camera (TMC)². However, certain anomalies like secondary craters affecting the age determination are more readily detected in radar datasets rather than optical dataset.

The ability of Mini-SAR to detect secondary craters and differentiate them from primary craters is because of the capability to utilize the polarimetric radar signatures.

Mini-SAR uses S-band (12.6 cm wavelength) to probe the far side, polar regions and particularly, the permanently shadowed region of the lunar surface. Mini-SAR contains two intensity images in H and V and two cross-power intensity images between the H and V exhibiting hybrid-polarity SAR where the transmitted field is circularly polarized, and the resulting backscatter is received in two mutually coherent linear polarizations³. The hybrid-polarity approach utilizes the polarized properties of the backscattered fields which are characterized as Stokes parameter⁴. The four channels of Mini-SAR were converted to Stokes parameters to generate the various daughter by-products to study the surface properties for detecting the secondary craters. The daughter by-products were noisy because of speckle; the image quality was improved by applying statistical filter followed by adaptive filters. MNF transformation was applied to the filtered images for reducing their coherent dimensionality and noise from the products. For surface dating, homogenous

cratered region was selected and the diameter of the craters within the area of interest was calculated for age dating.

Radar polarimetry has the capability to better distinguish between different types of surface and subsurface physical properties than single-polarization radar imagery⁵. Capability of radar to penetrate the surface and decipher the scattering properties based on the polarization information was used for deciphering the secondary craters. The study area was conducted on the lunar north polar region with its central selenographic coordinates at 83.6 lat. and –45.2 lon. on the lunar nearside (Figure 1a) near Sylvester crater.

Secondary craters were differentiated from primary craters based on their unique morphologies like high ellipticities, shallow profiles, tendency to form clusters and the occasional presence of herringbone or chevron-shape^{6–8}. In the study area, however, secondary craters arrangement does not necessarily attain the morphology as mentioned. Secondary craters formed from high impact velocity lack the characteristics such as flat, shallow floor of near-field secondaries and are difficult to differentiate solely through morphology.

In radar image, the secondary craters show higher circular polarization ratio